Journal of Directed Energy, **1**, Fall 2005, 241–260

Measurement of Gain in a Supersonic, Combustion-Driven Generator for NCl($a^1\Delta$)

Gerald C. Manke II* **and Timothy J. Madden**
Directed Energy Directorate, Air Force Research Laboratory, Kirtland Air Force Base, New Mexico 87117

Chris B. Cooper
Boeing–Rocketdyne, Kirtland Air Force Base, New Mexico 87117

and

Gordon D. Hager
Directed Energy Directorate, Air Force Research Laboratory, Kirtland Air Force Base, New Mexico 87117

The measurement of positive small signal gain on the 1.315-μm spin orbit transition of atomic iodine following energy transfer from chemically generated NCl($a^1\Delta$) is reported. Previous instances of gain produced by energy transfer from NCl($a^1\Delta$) used dc discharges to generate F and Cl atoms; this report describes recent progress toward a true chemical laser device that uses a high-temperature chemical combustor and a supersonic reactor to generate NCl($a^1\Delta$). These improvements represent a significant step toward the development and demonstration of a scalable All Gas-Phase Iodine Laser (AGIL) device.

KEYWORDS: AGIL, All gas iodine laser, Chemical lasers, COIL

1. Introduction

The All Gas-Phase Iodine Laser (AGIL)[17,18,25,26] is a laser device and concept that uses near-resonant energy transfer from an electronically excited molecule, NCl($a^1\Delta$), to ground-state atomic iodine to produce an inversion on the 1.3154-μm spin orbit transition of iodine:

$$NCl(a^1\Delta) + I(^2P_{3/2}) \rightarrow NCl(X^3\Sigma^-) + I^*(^2P_{1/2}). \quad (1)$$

AGIL is a potential all-gas-phase alternative to the chemical oxygen iodine laser (COIL), which uses the energy transfer between electronically excited oxygen, $O_2(a^1\Delta)$, and atomic iodine to produce $I^*(^2P_{1/2})$[33]:

$$O_2(a^1\Delta) + I(^2P_{3/2}) \rightarrow O_2(X^3\Sigma^-) + I^*(^2P_{1/2}). \quad (2)$$

Received January 19, 2005; revision received May 6, 2005.
*Corresponding author; e-mail: Gerald.Manke@Kirtland.af.mil.

It is possible to substitute $NCl(a^1\Delta)$ for $O_2(a^1\Delta)$ because both molecules possess a $(p\pi^*)^2$ $(p\sigma^*)^0$ electronic configuration (and therefore have the same electronic states), are metastable, and have large branching fractions for the near-resonant energy transfer to atomic iodine. While COIL is a relatively efficient laser (in terms of watts per kilogram and compared to other high-energy laser technologies), it suffers from complicated engineering challenges related to the use of two-phase chemistry in the production of $O_2(a^1\Delta)$. The reaction of molecular chlorine with an aqueous solution of basic hydrogen peroxide (BHP) produces $O_2(a^1\Delta)$ with near-unit efficiency:

$$Cl_2 + H_2O_2 + 2OH^- \rightarrow O_2(a^1\Delta) + 2H_2O + 2Cl^-, \tag{3}$$

but the use of the liquid-phase BHP and some unfavorable secondary chemistry [H_2O efficiently quenches $I^*(^2P_{1/2})$, $O_2(b^1\Sigma^+)$, and interferes with the I_2 dissociation process] leads to complex and severe problems for large-scale, high-energy devices, particularly those that require mobility. AGIL is attractive because $NCl(a^1\Delta)$ can be generated by reactions that occur solely in the gas phase.

The history and development of COIL has been well documented by McDermott,[32] Heaven,[14] and others.[37] The first continuous-wave AGIL device, demonstrated by Henshaw et al. in 2000,[17] was enabled and inspired by the work of many, including Benard et al.,[2] Bower et al.,[3,38] Clyne et al.,[4–6] Coombe et al.,[12,13,34–36] Heaven et al.,[14,21,22] Henshaw et al.,[15,16] Herbelin et al.,[18] Manke et al.,[27,28] and Setser et al.[10,19,20,30,31,39] Most recently, multiwatt laser demonstrations were performed by the AGIL team at the Air Force Research Laboratory (AFRL)[25,26] with a 20-cm-wide subsonic reactor that used a series of four dc discharges to produce the requisite F and Cl atoms. The highest gain and power measured on the 20-cm device were 4.2×10^{-4} cm^{-1} and 31 W (Ref. 24). In addition to the AFRL work, the Short Wavelength Chemical Laser Laboratory in Dalian, China, continues to pursue AGIL technology.[11]

Successful AGIL gain and laser demonstrations have produced $NCl(a^1\Delta)$ via a two-step reaction of chlorine atoms with hydrogen azide[20,27,30,31]:

$$Cl + HN_3 \rightarrow HCl + N_3, \tag{4}$$

$$Cl + N_3 \rightarrow NCl(a^1\Delta) + N_2. \tag{5}$$

The chlorine atoms were generated by the reaction of atomic fluorine and DCl:

$$F + DCl \rightarrow DF + Cl, \tag{6}$$

where the F atoms were generated by a dc discharge of molecular fluorine and/or NF_3 diluted in He. To improve the chemical efficiency of AGIL, small flows of hydrogen iodide are reacted with atomic fluorine or chlorine to produce $I(^2P_{3/2})$ prior to the reaction with hydrogen azide so that the $I(^2P_{3/2})$ atoms will be present as soon as $NCl(a^1\Delta)$ is produced:

$$F + HI \rightarrow HF + I(^2P_{3/2}), \tag{7}$$

$$Cl + HI \rightarrow HCl + I(^2P_{3/2}). \tag{8}$$

Unfortunately, the F atom production efficiency of the dc discharges declines as a function of the flow rate of the F-atom source[29]; the technology that was used previously to demonstrate the AGIL concept is not suitable for the development or demonstration of a kilowatt-scale device. This paper describes our efforts to generate $NCl(a^1\Delta)$, $I^*(^2P_{1/2})$ and observe small signal gain by using chemical combustor technology for the generation of $NCl(a^1\Delta)$.

2. Experimental Methods

2.1. Experimental apparatus

The supersonic AGIL device consisted of three major components, a subsonic $D_2/F_2/NF_3/DCl/HI$ combustor, a converging–diverging nozzle and HN_3 injector, and a supersonic flow chamber (Figs. 1 and 2). The combustion chamber measured 3.3 cm high, 5 cm wide, and 5.5 cm deep. Injectors for D_2 and F_2/NF_3 were located on the back wall of the combustion chamber. The D_2 injector consisted of two rows of six holes, each 0.038 cm in diameter. Molecular fluorine and nitrogen trifluoride were mixed upstream of the combustor and injected through a single row of six holes, each 0.132 cm in diameter. The D_2 injectors were located 0.38 cm above and below the row of F_2/NF_3 injector holes. The total injector areas for D_2 and F_2/NF_3 were 0.014 and 0.082 cm^2, respectively. The DCl and HI injectors were located on the top and bottom walls of the combustion chamber. The DCl injector block was placed 2.0 cm from the back wall and consisted of two rows (i.e., one row each for the top and bottom) of 36 holes, each 0.056 cm in diameter. The total DCl injector area was 0.177 cm^2. The HI injector was placed 3.5 cm from the back wall and consisted of two rows (i.e., one row each for the top and bottom) of 54 holes, each 0.033 cm in diameter. The total HI injector area was 0.0925 cm^2.

Three different supersonic nozzles were employed in this work. In all cases, the nozzle consisted of a 5-cm-wide slit, with the throat placed 7.0 cm from the back wall of the combustion chamber. Table 1 summarizes the details of the three nozzles used in this study. Nozzles A and B had a 0.46-cm throat height and 40-deg expansion angle. The throat for nozzle C was a factor of 2 smaller but maintained approximately the same A/A^* ratio (and Mach number) by having a smaller expansion angle, 20 deg. In all cases, the nozzle exit plane was placed 1.55 cm beyond the nozzle throat. Hydrogen azide was injected 0.4 cm downstream of the nozzle throat (i.e., 7.4 cm from the back wall of the combustion chamber) through two rows of 12 holes (one row each, top and bottom). The HN_3 injector holes for

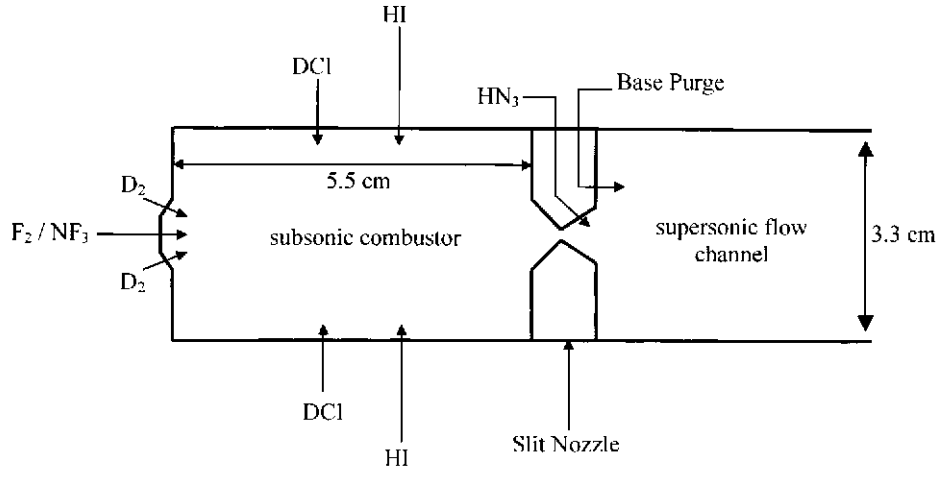

Fig. 1. Supersonic AGIL hardware. A side-view drawing of the experimental hardware is shown. The device consists of three regions: the subsonic combustor region, the converging–diverging slit nozzle, and the supersonic flow channel. See text for details.

Table 1. Supersonic AGIL nozzles

Nozzle	Throat height (cm)	Nozzle angle	Mach number[a] (Mach number)[b]	HN_3 injector area (cm^2) HN_3 injector hole diameter (cm)
A	0.46	40	3.6	0.195
			(3.2)	0.101
B	0.46	40	3.6	0.630
			(3.2)	0.183
C	0.23	20	3.6	0.630
			(3.2)	0.183

[a]Estimated from P/P_0 measurements and Eq. (14) assuming $\gamma = 1.667$.
[b]Calculated by iteratively solving Eq. (15) for M by using the measured A/A^* ratio and assuming $\gamma = 1.667$.

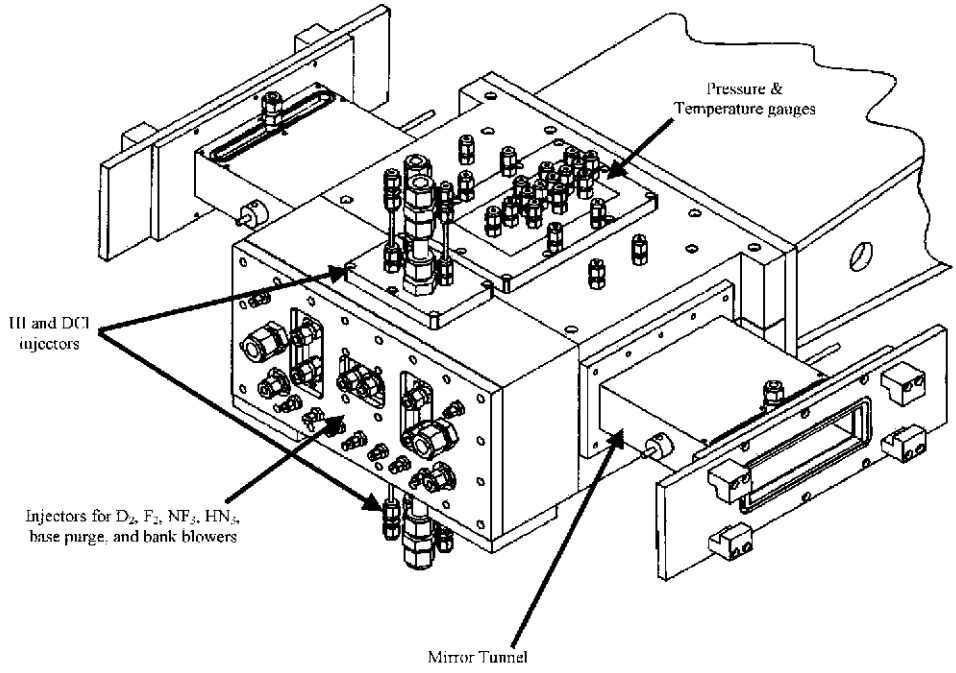

Fig. 2. Assembly drawing of supersonic AGIL reactor. Reagent feed lines and other major components are identified.

nozzle A were 0.102 cm in diameter, and the individual injector holes for nozzles B and C were 0.183 cm in diameter.

The supersonic flow chamber begins at the nozzle exit plane and extends downstream to the end of the reactor. The vertical height of the flow chamber was 3.3 cm. Because this height exceeds the height of the nozzle at the nozzle exit plane, a He injector was installed into the face of the nozzle to discourage recirculation of the reactive flow in the base purge region (Fig. 1). In addition to the base purge, a pair of supersonic ($M \geq 5$) bank blower

injectors were placed on either side of the nozzle to prevent expansion of the flow beyond the 5-cm width defined by the slit. Pitot probe measurements across the face of the nozzle confirmed flow containment and a 5-cm path length for the supersonic portion of the flow.

Mirror tunnels were constructed and attached to the sides of the reactor to allow flow visualization as well as small signal gain measurements. For most of the experiments described in this report, the mirror tunnels allowed observation of a 12-cm-long region of the flow. Based on the initial observation that the highest gain was found at the end of the 12-cm observation zone, a second pair of mirror tunnels was subsequently installed. The second set of tunnels provided a 25-cm-long observation zone. In both cases, a purge flow of He was added to each tunnel to help prevent damage by the corrosive gas to the glass windows.

All reagent and diluent flow rates except for HN_3 were controlled by Proportion Air electronic gas pressure regulators (Model QBIT-FEE-500) and calibrated sonic orifices. Pressures were monitored with MKS Baratron (Model 622-A) and Druck (PMP 1265) pressure transducers, and temperatures were measured with Omega (Type T) thermocouples. A National Instruments Labview program was used to control and record all reactor conditions for later analysis. The HN_3 flow was "controlled" by filling a pair of 150-liter stainless-steel tanks to a specified pressure with a mixture of 10% HN_3 in He and applying the full pressure of the tanks to the plenum of the HN_3 injectors. The average flow rate of HN_3 for each experiment was calculated from the measured pressure drop in the reservoir tanks. Typical flow rates are shown in Table 2. Typical conditions from previous AGIL devices are also given in Table 2 for comparison.

Table 2. Comparison of AGIL devices

	AGIL 1[18]	AGIL 1A[17]	AGIL 2[24,25]	Supersonic AGIL (this work)
		Reactor properties		
F atom source	1 dc discharge	1 dc discharge	4 dc discharges	$D_2/F_2/NF_3$ combustor
Flow speed	$M < 1$	$M < 1$	$M \sim 1$	$M \sim 3.5$
Path length (cm)	5	5	20	5
Pressure (torr)	16	15–16	20–30	200–350[a] 1–12[b]
Power (W)	NA	180 mW	31 W	NA
Gain (cm^{-1})	2.0×10^{-4}	2.6×10^{-4}	4.2×10^{-4}	1.2×10^{-4}
		Flow rates (mmol s^{-1})		
He	150	150	480–1,000	50–250[c]
F_2	0.66	NA	2–8	10
NF_3	NA	1–1.5	4–20	0–20
D_2	NA	NA	NA	2.5–20
DCl	2.0	2.0–2.5	15–25	30–70
HI	0.03	0.04–0.07	0.12–0.60	0.2–1.0
HN_3	3.32	3.0–4.5	10–70	10–70

[a]Static combustor pressure.

[b]Static pressure in supersonic flow channel.

[c]He added to combustor only; total He is sum of this value and nine times the HN_3 flow rate.

2.2. Diagnostics

Visible and near-infrared (NIR) emission spectra were observed with a 0.3-m monochromator (Acton, SpectroPro 300i) and a combination of two optical multichannel analyzers. The NIR emissions were collected with a liquid-nitrogen-cooled, 512-pixel InGaAs array (Roper Scientific, OMA V), and the visible emissions were collected with a

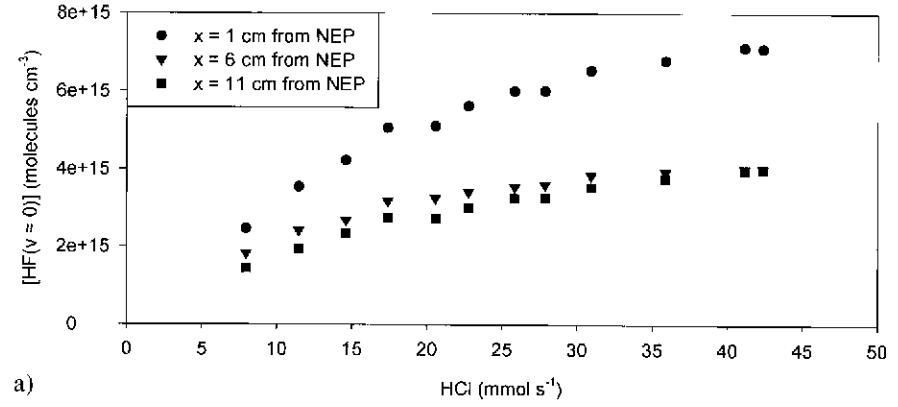

a)

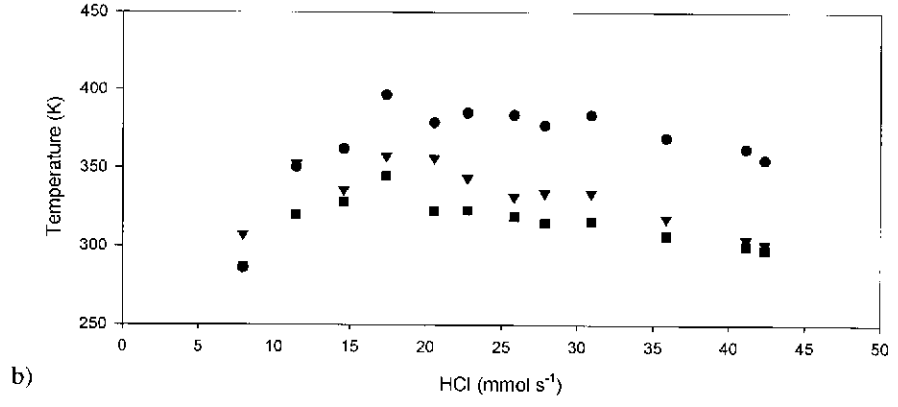

b)

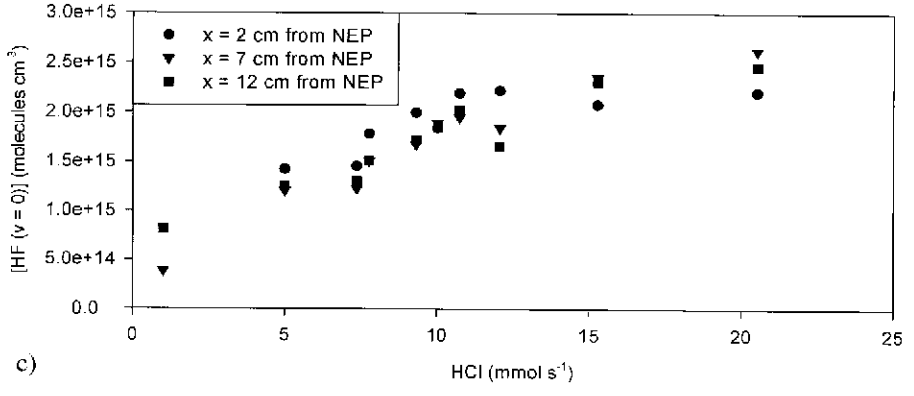

c)

liquid-nitrogen-cooled, 1,340 × 100 pixel charge-coupled device (CCD) (Roper Scientific, Spec 10:100BR). Binning the 100 pixels along the vertical axis created a single row of 1340 "superpixels." In addition to the spectroscopic measurements, a video camera provided visual images of the flow stream.

The F/Cl atom production efficiency was determined by a series of gas-phase titrations with HCl.[25] Briefly, a tunable external cavity diode laser (New Focus, Model 6248) was tuned to the P(3) ro-vibrational line of the HF(0-2) overtone spectrum; the absorption was measured as a function of HCl added to the high-temperature combustor. The absorption increases linearly with HCl until all of the F atoms are consumed. The titration endpoint is reached when additions of HCl no longer lead to increased absorption and the initial F atom flow rate is equal to the corresponding HCl flow rate. The small signal gain on the $I(^2P_{3/2})$–$I^*(^2P_{1/2})$ transition was monitored by the same diode laser tuned to the F(3,4) hyperfine transition. The initial I-atom density was measured prior to any HN_3 addition to determine $[I_{tot}]$.

Finally, a tunable 664-nm diode laser was used to probe the density of NCl($X^3\Sigma^-$). This diagnostic device was developed and delivered to the AFRL via a Phase II SBIR contract with Physical Sciences, Inc.[9] The laser was continuously scanned from 15,049 to 15,050 cm^{-1} (664.46–664.48 nm) through a spectral region that contains two hyperfine lines of the NCl($X^3\Sigma^-$)–NCl($b^1\Sigma^+$) spectrum,[22] $^QR^{34}$ and ^QP.[34] The absolute wavelength and frequency axis of the spectrum were calibrated by simultaneously collecting a high-resolution spectrum of molecular I_2. The density of NCl($X^3\Sigma^-$) is calculated from the integrated absorption area and the calculated value for the transition-specific line strength.[9]

3. Experimental Results

3.1. F-atom titrations

Gas-phase titrations were performed as described above in an attempt to determine the initial F-atom density produced by the high-temperature combustor. Unfortunately, the results were not nearly as satisfying as those generated in the subsonic experiments. Sample titrations are shown in Fig. 3. The upper panel shows the results for nozzle A and $F_2 = 12$, $D_2 = 10$, $NF_3 = 5$, and He = 125 mmol s^{-1}. A slight break to the linear growth of the absorption signal normally indicates the titration endpoint. For the experimental series shown in the upper panel, the break occurs at ~17 mmol s^{-1}.

A simple $D_2/F_2/NF_3$ combustion mechanism may be constructed from the following three net reactions:

$$D_2 + F_2 \rightarrow 2DF + \text{heat}, \tag{9}$$

Fig. 3. F + HCl titrations: (a) The measured density of HF(0) is plotted as a function of HCl added to the $F_2/NF_3/D_2$ combustor and nozzle A. The experimental conditions were $F_2 = 12$, $D_2 = 10$, $NF_3 = 5$, and He = 125 mmol s^{-1}. The static cavity (sidewall) pressure was 1.5 torr. The HF($v = 0$) density was measured at three different downstream positions, and the titration endpoint is given by the slight break in the slope at HCl ~ 17 mmol s^{-1}. (b) The gas temperature is determined from the linewidth of the HF spectrum and is shown as a function of HCl. (c) A second titration is shown for nozzle C and $F_2 = 10$, $D_2 = 7.5$, $NF_3 = 0$, and He = 10 mmol s^{-1}.

$$F_2 + \text{heat} \rightarrow 2F, \tag{10}$$

$$NF_3 + \text{heat} \rightarrow 3F + N. \tag{11}$$

This model allows us to calculate the maximum molar flow rate of F atoms that can be generated by the combustor:

$$F_{max} = 2(F_2) + 3(NF_3) - 2(D_2). \tag{12}$$

For the conditions of the upper panel, $2F_2 + 3NF_3 - 2D_2 = 19$ mmol s^{-1}, and the titration endpoint of HCl = 17 mmol s^{-1} indicates 89% dissociation. However, because the titrant HCl is added into the very chemically complex combustor region, there is significant opportunity for secondary chemistry and systematic error. This possibility was realized in experiments summarized in the lower panel of Fig. 3. In this case, a titration is shown for nozzle C and $F_2 = 10.0$, $D_2 = 7.5$, $NF_3 = 0$, and He = 10 mmol s^{-1}. The simple $D_2/F_2/NF_3$ combustion model predicts $F_{max} = 5$ mmol s^{-1}. In stark contrast, the titration endpoint occurs at HCl = 10 mmol s^{-1}, suggesting an impossible value of 200% dissociation efficiency. Yet another set of titrations (not shown) for nozzle C and $F_2 = 10$, $NF_3 = 0$, and He = 100 mmol s^{-1} indicated a titration endpoint of F ~ 35 mmol s^{-1} for both $D_2 = 7.5$ and $D_2 = 15$ mmol s^{-1}. Assuming complete $D_2/F_2/NF_3$ combustion, the highest possible F-atom flow rates for these conditions are 20 and 35 mmol s^{-1}, respectively.

The observations of titration endpoints being independent of the D_2 flow rate and theoretically impossible dissociation efficiencies are strong evidence that the assumptions underlying the titration experiments are false and that this method is not a robust diagnostic for determining $[F]_0$ and/or $[Cl]_0$. Almost certainly, HCl/DCl, NF_3, and HI participate in the D_2/F_2 chemistry and the result is a very complex mixture. Hence, subsequent experiments that involved the addition of HN_3 were always performed with DCl = 70 mmol s^{-1}, a flow rate well in excess of the theoretical maximum F-atom flow rate.

Despite the ambiguity of the initial F/Cl flow rate, the titration data were extremely valuable for characterizing device performance. Analysis of the spectral lineshapes allows the generation of temperature plots such as the one shown in the middle panel of Fig. 3. (Interestingly, the temperature in the cavity also reaches a maximum value at HCl ~17 mmol s^{-1}.) Unlike the [HF] vs HCl titration data, the temperature data are robust because the underlying chemistry that generates the heat is not important. Furthermore, the cavity temperature data can be used to calculate the combustor temperature. The isentropic equation for the ratio between the stagnation and static temperature is

$$\frac{T_0}{T} = \left(1 + \frac{\gamma - 1}{2} M^2\right), \tag{13}$$

where T_0 is the stagnation temperature, T is the static cavity temperature, γ is the specific heat ratio (C_p/C_v), and M is the Mach number. The Mach number is given by the ratio of the stagnation and static pressures and Eq. (14):

$$M = \sqrt{\frac{2}{\gamma - 1}\left[\left(\frac{P_0}{P}\right)^{(\gamma - 1)/\gamma} - 1\right]}, \tag{14}$$

where P_0 is the stagnation (plenum) pressure and P is the static (cavity sidewall) pressure. For nozzles A and B, typical values for P_0 and P are 100 and 1.6 torr, respectively. Assuming $\gamma \leq 1.667$, Eq. (14) gives $M \sim 3.6$ (in the absence of HN_3). This value is slightly larger than the value predicted by the nozzle area ratio (Table 1) at the nozzle exit plane and

Eq. (15):

$$\frac{A}{A^*} = \frac{1}{M}\left[\left(\frac{2}{\gamma+1}\right)\left(1+\frac{\gamma-1}{2}M^2\right)\right]^{(\gamma+1)/2(\gamma-1)} \tag{15}$$

This is not surprising because of the large base relief region beyond the nozzle exit plane (NEP); freejet expansion of the flow leads to higher Mach numbers. According to the titration data, the static temperature is 350–400 K for nozzles A and B, which gives $T_0 = 1{,}900$–$2{,}100$ K. For nozzle C, typical stagnation and static (sidewall) pressures are 380 and 6.6 torr, respectively, and Eq. (14) again gives $M \sim 3.6$. A stagnation temperature for nozzle C of 1,300–1,600 K is calculated from Eq. (13) and the titration data, which gives $T = 250$–300 K.

3.2. Emission spectra

To confirm the presence of NCl($a^1\Delta$), NCl($b^1\Sigma^+$), and $I^*(^2P_{1/2})$, a series of emission spectra were collected (Fig. 4). The upper panel was collected with the OMA V camera and clearly indicates the presence of these species and the absence of any strong extraneous emissions. This visible emission spectrum, collected with a CCD focal plane array, is shown in the middle panel. It is important to note that the visible portion of the spectrum shown in the upper panel is weak because the OMA V instrument has a poor response at 665 nm. The experimental conditions were $F_2 = 10$, $D_2 = 15$, $NF_3 = 10$, DCl = 70, HI = 0.2, and $HN_3 = 25$ mmol s^{-1}. The $I^*(^2P_{1/2})$ signal is quite strong and saturates the camera at this resolution (i.e., slit width). A spectrum collected at a slit width that does not saturate the detector is shown in the lower panel. Under these conditions, the ratio of the $I^*(^2P_{1/2})$ and NCl($a^1\Delta$) spectral areas is approximately 60:1. Since the radiative lifetimes[1,7,8] for NCl($a^1\Delta$) and $I^*(^2P_{1/2})$ are 2.7 and 0.2 s, respectively, and the detector response function is flat across this region, this ratio corresponds to a [NCl($a^1\Delta$)]:[$I^*(^2P_{1/2})$] ratio of 0.23. While the very intense $I^*(^2P_{1/2})$ emission is encouraging, the low [NCl($a^1\Delta$)]:[$I^*(^2P_{1/2})$] ratio is problematic, especially for an energy transfer laser. Spectra collected in the absence of HN_3 show weak, transient signals at 1,050, 1,200, and 1,300 nm. The 1,300-nm signal is readily assigned to HF($\Delta v = 2$) emission, but the other features are not immediately identifiable. The transient nature of the emissions (they disappear after a few seconds) and the simultaneous appearance of HF overtone emission suggest that they are related to the combustion process, possibly NF* or NF_2^*.

3.3. Small signal gain measurements

As demonstrated in the preceding section, addition of HN_3 to the combustor products generated NCl($a^1\Delta$) and $I^*(^2P_{1/2})$. Under a variety of conditions, we were also able to observe positive small signal gain (Figs. 5–8). Figure 5 shows two examples of inversion on the $I(^2P_{3/2})$–$I^*(^2P_{1/2})$ transition. The conditions for the upper panel were $F_2 = 10$, $D_2 = 7.5$, $NF_3 = 22$, DCl = 50, HI = 0.25, and He = 210 mmol s^{-1}. Nozzle B was used, and the cavity pressure increased from 6.8 to 9.8 torr upon addition of 42 mmol s^{-1} of HN_3 and 381 mmol s^{-1} of He. As the data show, the small iodine absorption signal is converted to positive gain upon the addition of HN_3. The positive gain was observed at $x = 11$ cm from the NEP; the signals at $x = 1$ and 6 cm, on the other hand, exhibited optical transparency. Optimized data from experiments with nozzle C (see below) are shown in the lower panel.

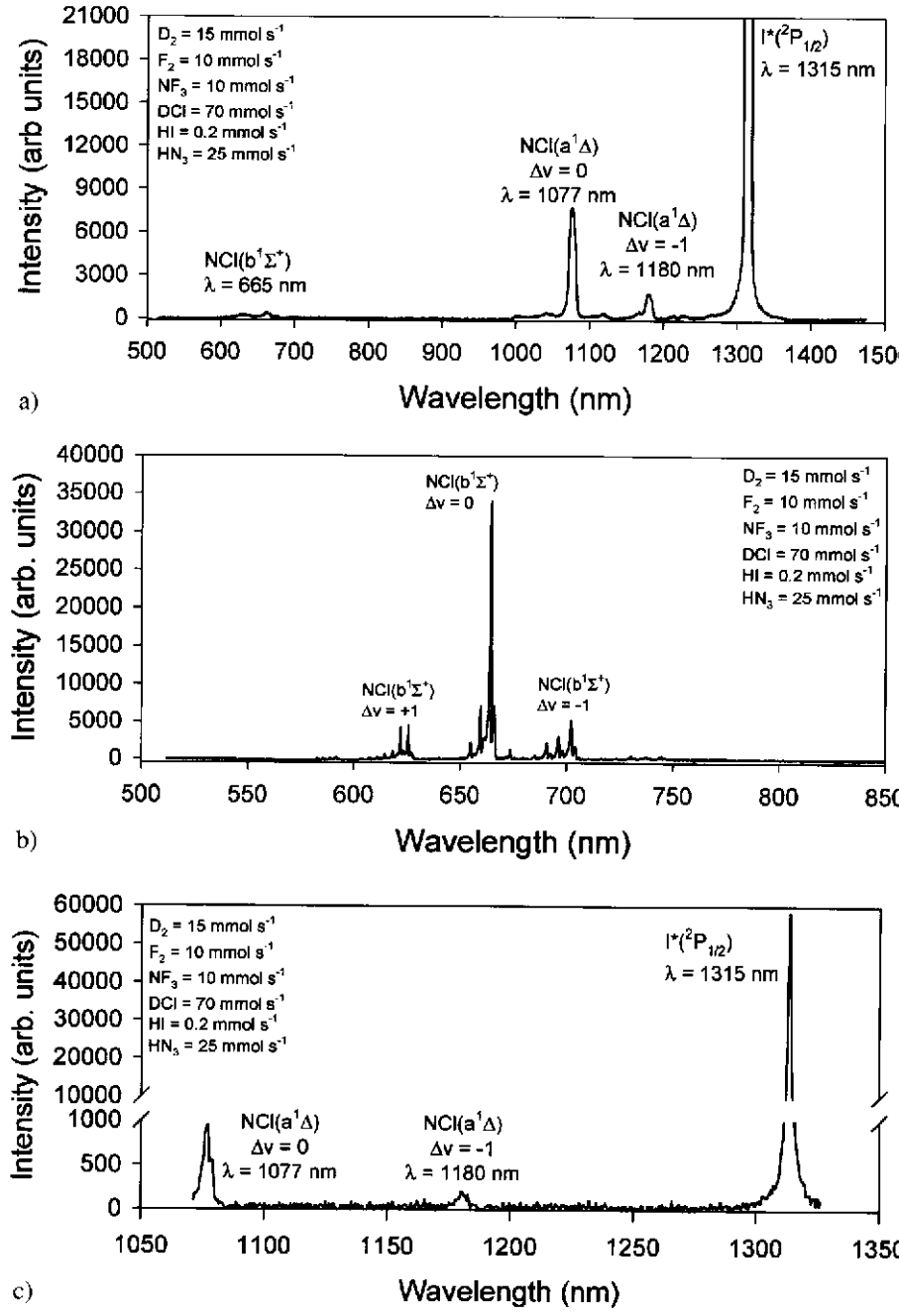

Fig. 4. Emission spectra: (a) Visible and near-IR emissions resulting from full AGIL chemistry as detected by an OMA V detector. Note that the $I^*(^2P_{1/2})$ signal has saturated the camera and that the NCl($b^1\Sigma^+$) signal is weak due to the poor response of the OMA V at this wavelength. (b) Visible and NIR emissions as detected with a CCD system. (c) Relative (unsaturated) intensities of the NIR NCl($a^1\Delta$) and $I^*(^2P_{1/2})$ emissions.

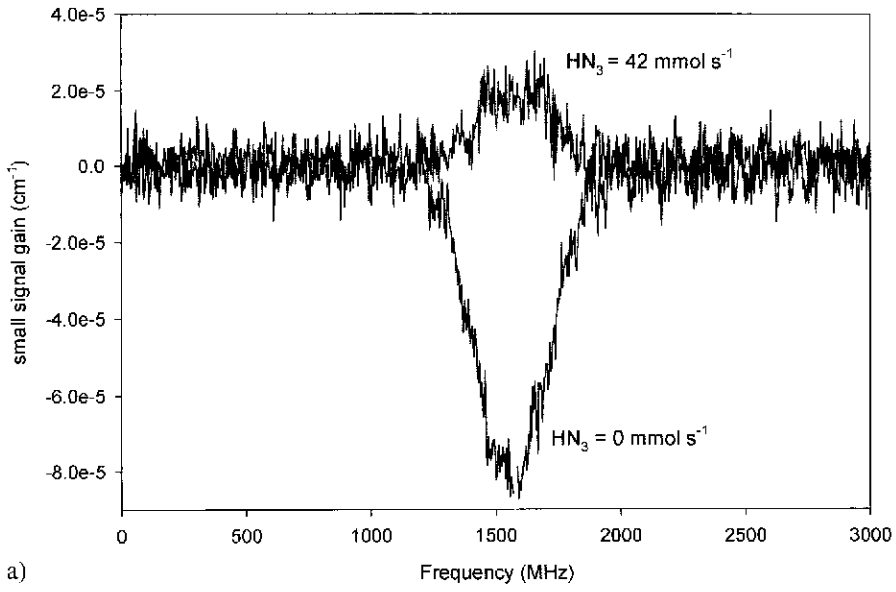

a)

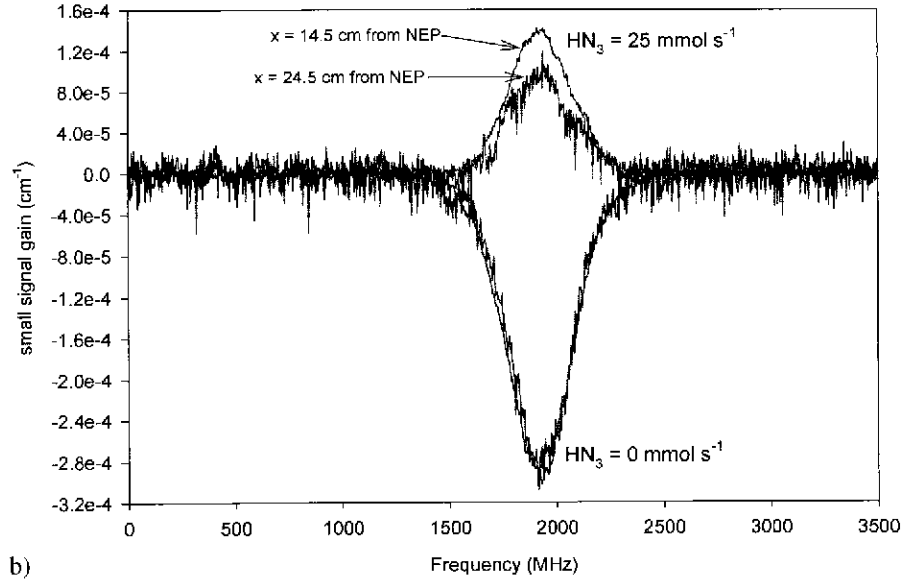

b)

Fig. 5. Absorption/gain spectra: (a) Demonstration of inversion from nozzle B and $F_2 = 10$, $D_2 = 7.5$, $NF_3 = 22$, DCl = 50, HI = 0.25, and He = 210 mmol s^{-1}. Gain is achieved upon the addition of 42 mmol s^{-1} of HN_3. The peak gain, observed at $x = 11$ cm downstream of the NEP, is 2.1×10^{-5} cm^{-1}, corresponding to 43% inversion. (b) Gain demonstrations at the optimized conditions for nozzle C. The conditions were $F_2 = 10$, $D_2 = 15$, $NF_3 = 15$, DCl = 70, HI = 0.50, and He = 110 mmol s^{-1}. Positive gain is observed at $x = 14.5$ and 24.5 cm upon the addition of $HN_3 = 25$ mmol s^{-1}. In this case, the peak gain is 1.4×10^{-4} cm^{-1} (i.e., 45% inversion).

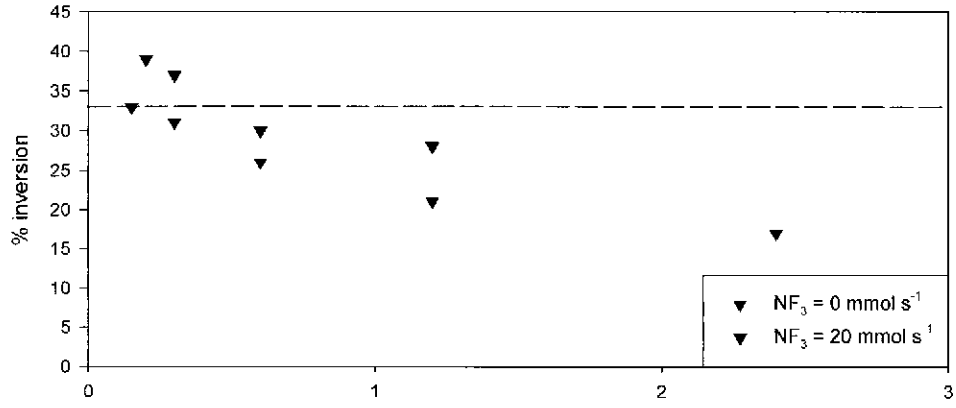
% inversion
HI (mmol s-1)
NF3 = 0 mmol s-1
NF3 = 20 mmol s-1

a)

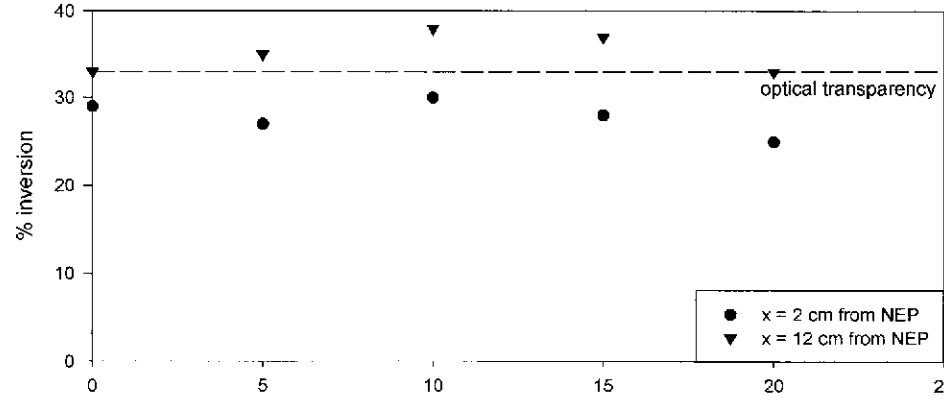
% inversion
NF3 (mmol s-1)
optical transparency
x = 2 cm from NEP
x = 12 cm from NEP

b)

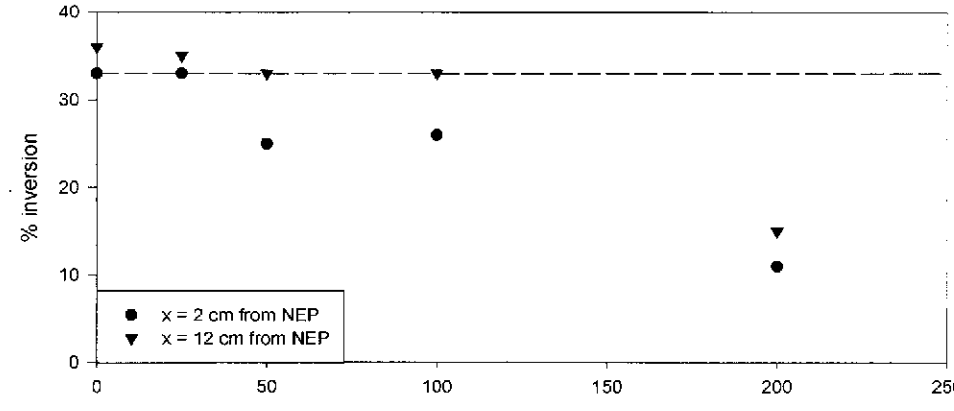
% inversion
He diluent to DCI line (mmol s-1)
x = 2 cm from NEP
x = 12 cm from NEP

c)

The conditions were similar to those used in the upper panel: $F_2 = 10$, $D_2 = 15$, $NF_3 = 15$, DCl = 70, HI = 0.5, and He = 110 mmol s^{-1}. In addition, the tunnel purge flow was increased from a typical value of 250 to 1,000 mmol s^{-1}. The small signal gain was observed to be as high as 1.4×10^{-4} cm^{-1} upon addition of 25 mmol s^{-1} of HN_3 and 278 mmol s^{-1} of diluent He. In this case, an extended observation zone was used and gain was observed at $x = 14.5$ and 24.5 cm from the nozzle exit plane.

Numerous series of experiments were conducted to optimize the small signal gain as a function of the starting conditions. Examples are shown in Figs. 6–8. Unless indicated otherwise, the data shown were generated with nozzle C. Because the addition of NF_3, HI, and other reagents interferes with the combustion process, the value for $[I_{tot}]$ may vary with the specific combustor conditions. Hence, each gain measurement was accompanied by a measurement of $[I(^2P_{3/2})]$ in the absence of HN_3. Furthermore, the gain data are plotted as percent inversion, where

$$\% \text{ inversion} = \frac{[I^*(^2P_{1/2})]}{[I_{tot}]} \times 100\% \tag{16}$$

and inversion >33% indicates positive gain. The upper, middle, and lower panels of Fig. 6 show inversion plotted as a function of HI, NF_3, and He diluent to the DCl flow, respectively. The upper and middle panels of Fig. 7 demonstrate the dependence on D_2 and HN_3, respectively, while the lower panel of Fig. 7 shows a vertical profile of the flow. Finally, Fig. 8 shows percent inversion vs Δt and the tunnel purge flow rate.

The experimental conditions for the upper panel of Fig. 6 were $F_2 = 10$, $D_2 = 7.5$, DCl = 70, He = 110, $NF_3 = 0$ or 20, and $HN_3 = 25$ mmol s^{-1}. The data shown were collected at $x = 12$ cm from the NEP. The data clearly show that gain decreases with added HI. Since HI is added upstream of the nozzle where F and Cl atoms are the main species, the HI is rapidly converted to iodine atoms. The decreasing gain is consistent with rapid depletion of [NCl($a^1\Delta$)] by iodine atoms via energy transfer. The data also indicate that the addition of NF_3 is beneficial, most likely because higher $[F]_0$ leads to higher $[Cl]_0$, which in turn leads to faster NCl($a^1\Delta$) production.

The middle panel of Fig. 6 further demonstrates the dependence of the inversion on the NF_3 flow rate. The conditions for this experimental series were $F_2 = 10$, $D_2 = 7.5$, DCl = 70, HI = 0.2, He = 110, and $HN_3 = 25$ mmol s^{-1}. The highest observed gain for this plot, 5.1×10^{-5} cm^{-1}, was measured at $x = 12$ cm from the NEP. This value corresponds to 38% inversion.

The lower panel of Fig. 6 demonstrates the effect of diluent added to the combustor. For this series, $F_2 = 10$, $D_2 = 7.5$, $NF_3 = 20$, DCl = 70, HI = 0.2, and $HN_3 = 25$ mmol s^{-1}. The data for $x = 2$ and 12 cm from the NEP are shown. The level of inversion decreases as He

Fig. 6. Inversion vs HI, NF_3, and combustor He diluent: (a) The extent of the inversion of the iodine-atom transition is plotted as a function of HI and two different values of the NF_3 flow rate. The experimental conditions were $F_2 = 10$, $D_2 = 7.5$, DCl = 70, He = 110, and $HN_3 = 25$ mmol s^{-1}. (b) Positive gain (i.e., inversion > 33%) is achieved for $NF_3 = 5$–15 mmol s^{-1} and constant $F_2 = 10$, $D_2 = 7.5$, DCl = 70, HI = 0.2, He = 110, and $HN_3 = 25$ mmol s^{-1}. (c) Effect of diluent added to the combustor. For this series, $F_2 = 10$, $D_2 = 7.5$, $NF_3 = 20$, DCl = 70, HI = 0.2, and $HN_3 = 25$ mmol s^{-1}. See text for details.

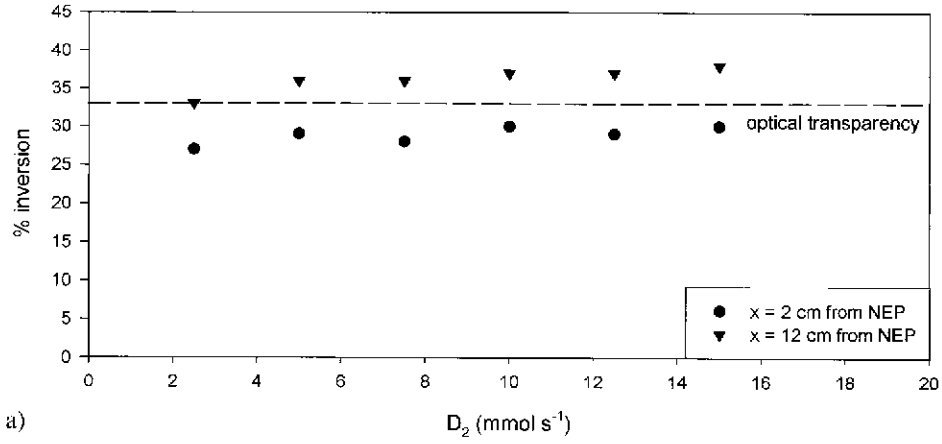
% inversion
optical transparency
x = 2 cm from NEP
x = 12 cm from NEP
D_2 (mmol s^{-1})

a)

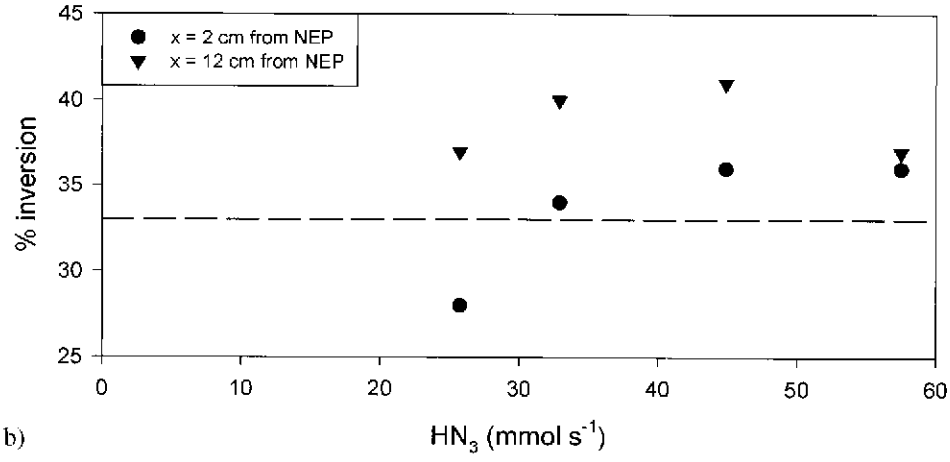
% inversion
x = 2 cm from NEP
x = 12 cm from NEP
HN_3 (mmol s^{-1})

b)

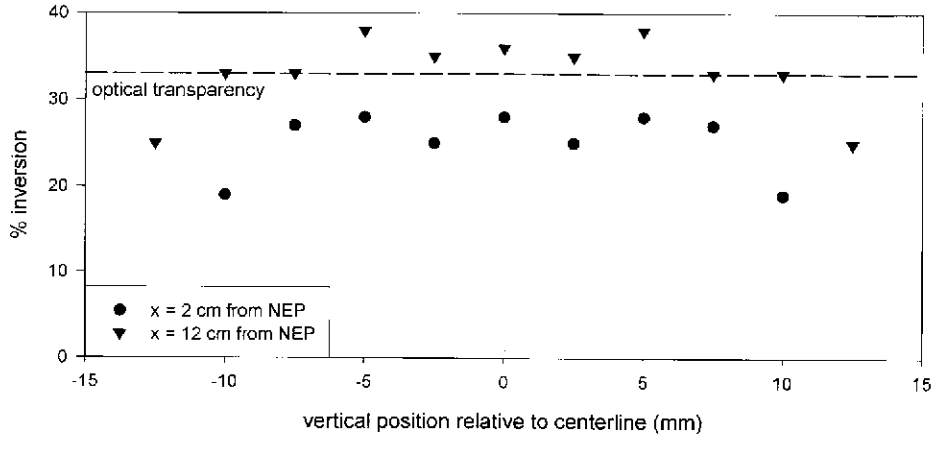
% inversion
optical transparency
x = 2 cm from NEP
x = 12 cm from NEP
vertical position relative to centerline (mm)

c)

is added (in this case as a diluent to the DCl). Simultaneously measured temperature data (not shown) also indicate a concomitant decrease in the temperature with added He. One plausible explanation for the decreasing gain is that the rate-determining step for NCl($a^1\Delta$) production, reaction (4), is strongly temperature dependent. Less NCl($a^1\Delta$) is generated as the combustor and cavity temperatures decrease due to the addition of room-temperature He to the combustor.

The upper panel of Fig. 7 plots percent inversion as a function of the D_2 flow rate. The base conditions for this series are $F_2 = 10$, $NF_3 = 10$, $DCl = 70$, $HI = 0.2$, $He = 110$, and $HN_3 = 25$ mmol s^{-1}. Interestingly, the gain is relatively constant for $D_2 = 5$–15 mmol s^{-1}. This observation is consistent with the unsatisfactory results of the titration experiments. In principle, excess D_2 should consume more of the atomic and molecular fluorine and lead to a net decrease in the density of Cl atoms available for reaction with HN_3. To date, we have no satisfactory explanation for this observation. Clearly, future AGIL devices will require a careful and thorough examination of the combustor chemistry and design. Unfortunately, such a study was beyond the scope of this work.

The middle panel of Fig. 7 shows the very important relationship between gain and the HN_3 flow rate. The experimental conditions for this plot are $F_2 = 10$, $D_2 = 15$, $NF_3 = 10$, $HI = 0.2$, $DCl = 70$, and $He = 110$ mmol s^{-1}. This relationship is an important indicator of the overall efficiency of AGIL chemistry; if the HN_3 flow rate greatly exceeds the estimated Cl atom flow rate (or vice versa), this would constitute evidence for poor $HN_3 \rightarrow$ NCl($a^1\Delta$) conversion and/or poor mixing. The optimum inversion occurs for $HN_3 \sim 45$ mmol s^{-1}. Assuming strict stoichiometric combustor chemistry, the highest possible Cl atom flow rate is 35 mmol s^{-1}. Hence, the upper bound for the Cl:HN_3 ratio is 0.77. Since each NCl($a^1\Delta$) molecule requires two Cl atoms to produce, stoichiometry states that the Cl:HN_3 ratio should be 2. It is important to point out that because we were unable to unambiguously measure $[Cl]_0$, this ratio is an upper bound. Furthermore, this upper bound is slightly higher than, but not inconsistent with, the subsonic experiments; AGIL 1 and AGIL 2 had Cl:HN_3 ratios of 0.25 and 0.40, respectively.

The lower panel of Fig. 7 shows a vertical profile of the gain measured for nozzle C and $F_2 = 10$, $D_2 = 7.5$, $NF_3 = 10$, $DCl = 70$, $HI = 0.2$, $He = 110$, and $HN_3 = 25$ mmol s^{-1}. The I-atom absorption and gain were measured along the vertical axis of the reactor in 2.5-mm steps. Because symmetry about the vertical axis was assumed, the data shown for the region above the vertical centerline are the same as the measured values from below the vertical centerline. Interestingly, the gain persists for ± 5 mm beyond the vertical centerline and optical transparency persists another ± 5 mm. The actual nozzle half-height at the nozzle

Fig. 7. Inversion vs D_2, HN_3, and vertical profile: (a) Percent inversion plotted as a function of the D_2 flow rate. For this series $F_2 = 10$, $NF_3 = 10$, $DCl = 70$, $HI = 0.2$, $He = 110$, and $HN_3 = 25$ mmol s^{-1}. The gain does not appear to have a strong dependence on D_2 over the range tested. (b) Relationship between percent inversion and HN_3 flow rate. The experimental conditions for this plot are $F_2 = 10$, $D_2 = 15$, $NF_3 = 10$, $HI = 0.2$, $DCl = 70$, and $He = 110$ mmol s^{-1}. (c) Vertical profile of the gain measured for nozzle C and $F_2 = 10$, $D_2 = 7.5$, $NF_3 = 10$, $DCl = 70$, $HI = 0.2$, $He = 110$, and $HN_3 = 25$ mmol s^{-1}. Because symmetry about the vertical axis was assumed, the data shown for the region above the vertical centerline are the same as the measured values from below the vertical centerline.

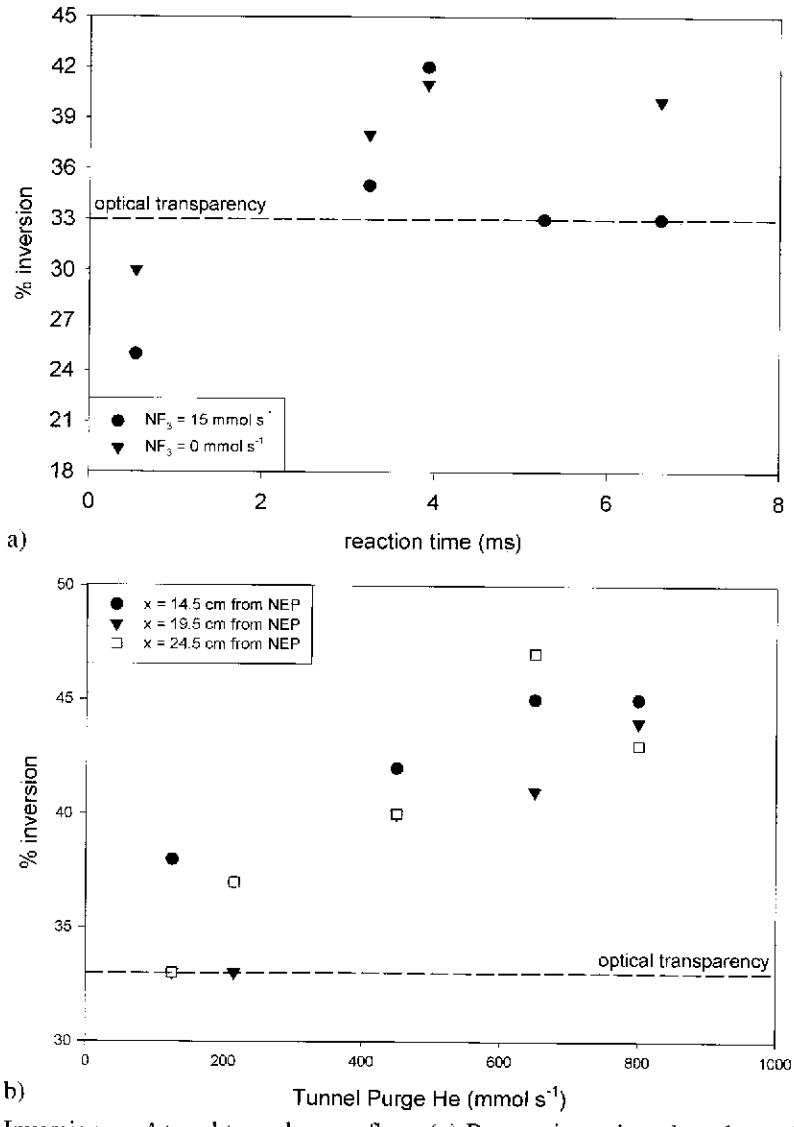

Fig. 8. Inversion vs Δt and tunnel purge flow: (a) Percent inversion plotted as a function of reaction time. The reaction time is calculated from the observation position relative to the NEP and the estimated gas velocity (3,700 cm s^{-1}). Results are shown for two different NF_3 flow rates and for constant $D_2 = 15$, $F_2 = 10$, DCl = 70, HI = 0.2, He = 110, and $HN_3 = 25$ mmol s^{-1}. (b) Percent inversion plotted as a function of the tunnel purge He flow rate. The experimental conditions were $D_2 = 15$, $F_2 = 10$, $NF_3 = 15$, DCl = 70, HI = 0.3, He = 110, and $HN_3 = 25$ mmol s^{-1}.

exit plane is 4 mm from the centerline: expansion of the flow into the base purge region is evident but does not appear to be a major problem. A vertical profile of the flow generated by nozzles A and B was also performed. The data (not shown) were collected for $F_2 = 12.5$, $D_2 = 5.0$, and He = 120 mmol s^{-1}. [In this case, HF(2-0) rather than I atom absorptions were

measured along the vertical centerline.] While expansion of the flow into the base purge region was slightly more pervasive for this series, the bulk of the flow remained within ±8 mm of the vertical centerline, even at the point farthest downstream that was probed.

The temporal profile of the $I^*(^2P_{1/2})$–$I(^2P_{3/2})$ inversion density is shown in the upper panel of Fig. 8. The data points for this plot were collected at the same conditions but were separated in time by several weeks. It is important to note that the reaction time axis is only approximate because the bulk gas velocity was used to calculate Δt. The bulk gas velocity, $v_{gas} \sim 3{,}700\ \mathrm{cm\ s^{-1}}$, was estimated from $\gamma = 1.667$, molecular weight (MW) = 4.0, $M = 3.5$, and Eq. (17):

$$v_{gas} = M^* \sqrt{\frac{\gamma RT}{MW}}. \tag{17}$$

The data indicate a rapid increase in the gain between 0 and 4 ms, followed by a plateau region between 4 and 8 ms.

Finally, in the lower panel of Fig. 8, inversion density is plotted as a function of the tunnel purge flow. The gain increases dramatically as the purge flow is increased. There are at least two possible explanations for this behavior. First, the increased purge flows may be compressing the flow along the direction of the optical axis. This would lead to slightly higher densities and slightly higher temperatures, both of which can lead to faster and more efficient NCl(a$^1\Delta$) production. The second explanation involves the possibility of shocks generated by the extra He flow in the downstream portion of the flow reactor. This would lead to a slower flow and a lower Mach number. In either case, the data suggest that even better performance may be achieved by building a supersonic nozzle with a lower A/A^* ratio and Mach number.

3.4. Attempts to detect NCl($X^3\Sigma$)

The NCl($X^3\Sigma^-$) diagnostic uses a ratiometric detection scheme to eliminate noise associated with fluctuations of the laser intensity. This enables very low absorption signals to be measured[9]; calibrations performed at PSI with molecular I_2 found that absorptions as low as 10^{-4} could be measured by this instrument with a reasonable signal-to-noise ratio. Given the NCl($X^3\Sigma^-$)–NCl($b^1\Sigma^+$) absorption line strength factor of 1.53×10^{-19} cm molecule^{-1} and a single-pass path length of 5 cm, an easily observable absorption of $\sim 3.5 \times 10^{-3}$ should be produced by $[NCl(X^3\Sigma^-)] = 1 \times 10^{14}\ \mathrm{cm^{-3}}$.

An estimate for the density of NCl($X^3\Sigma^-$) in our device can be made by using the data from the small signal gain measurements. According to Eq. (1), each $I^*(^2P_{1/2})$ atom is accompanied by the generation of an NCl($X^3\Sigma^-$) molecule. Given a typical $[I_{tot}] \leq 1 \times 10^{14}\ \mathrm{cm^{-3}}$ and optimum gain of $1 \times 10^{-4}\ \mathrm{cm^{-1}}$ (i.e., inversion $\leq 45\%$), $[I^*(^2P_{1/2})] = [NCl(X^3\Sigma^-)] \leq 4.5 \times 10^{13}\ \mathrm{cm^{-3}}$ is calculated. This value will be larger if significant amounts of NCl($X^3\Sigma^-$) are generated by additional collisional quenching or directly by reaction (5). It will be lower, on the other hand, if the energy transfer or other quenching reactions produce significant quantities of NCl($X^3\Sigma^-$, $v \neq 0$) or if there are rapid reactions that consume NCl($X^3\Sigma^-$). Ground-state NCl densities on the order of $(2\text{–}4) \times 10^{13}\ \mathrm{cm^{-3}}$ should be sufficient to generate a resolvable absorption signal, albeit rather weakly. Surprisingly, attempts to measure NCl($X^3\Sigma^-$) under the operating conditions of nozzles A–C showed no evidence of absorption. The lack of an observable signal is puzzling and suggests that NCl($X^3\Sigma^-$, $v = 0$) is a very minor component of the flow or that NCl($X^3\Sigma^-$) is eliminated by chemical reaction on a very fast timescale.

4. Discussion and Conclusions

Multiple conclusions and trends are evident from these data and experiments. The first is that the AGIL chemistry is robust: quantities of $NCl(a^1\Delta)$ and small signal gain values sufficient for lasing can be generated by using technology that has been proven to be scalable by the HF laser community.[23] In particular, we have proven that a high-temperature chemical combustor can be used as a source of Cl atoms and that small signal gain can be generated upon supersonic expansion and the addition of HN_3.

In addition, this work has identified where the focus of future work should be placed in order to enable and demonstrate a high-energy (i.e., multikilowatt) laser system. Specifically, the future utility of AGIL depends on designing a nozzle that creates the optimal reaction conditions in the supersonic flow region but also allows efficient mixing of the HN_3 fuel. Nozzles A and B, for example, produced a supersonic flow with $T = 400$–500 K. According to temperature-dependent rate constant measurements and the previous subsonic AGIL work,[25,27] this is nearly optimal for $NCl(a^1\Delta)$ formation. Unfortunately, nozzles A and B gave rather poor penetration and mixing of HN_3. Inspections of the visible chemiluminescence showed two bright red flames that began at the HN_3 injectors and extended beyond the observation region downstream. The vertical centerline of the reactor remained dark, indicating the absence of $NCl(b^1\Sigma^+)$ [and, by inference, $NCl(a^1\Delta)$] for all but the highest HN_3 flow rates. On the other hand, full penetration of the HN_3 into the main flow was achieved with the smaller throat height and shallower expansion angle nozzle C, but in this case the initial temperature was only ~250 K, too low for fast, efficient generation of $NCl(a^1\Delta)$. Furthermore, enhancements to the observed gain were achieved when the Mach number was decreased (Fig. 8). It is clear that future generations of AGIL technology must pay careful attention to the details of the supersonic nozzle in order to optimize the generation rate of $NCl(a^1\Delta)$.

A second challenge for future AGIL devices is tied to the laser fuel, HN_3. Because of its potential (some would say propensity) for explosive decomposition, the storage and dynamic pressure of HN_3 must be kept low. For example, while the vapor pressure for HN_3 at room temperature is nearly 400 torr, safety concerns limit the practical storage partial pressure to only 100–200 torr. Since the degree of penetration depends on the pressure difference between the plenum pressure of the injected fluid and the static pressure of the main flow, the HN_3 must be highly diluted in order to get the plenum pressure to an acceptable level. Unfortunately, the addition of large flows to the supersonic fluid can lead to shocks or even unchoke the supersonic nozzle. Just as important, the need for low-pressure storage of HN_3 leads to highly inefficient storage systems. In our case, the HN_3 is stored in six 150-liter tanks. These tanks consume a significant amount of laboratory space, take three to four days to fill, and are sufficient only for a single day of experiments. Clearly, future generations of AGIL technology must incorporate a more compact, efficient, and sustainable HN_3 generation and delivery system.

Despite these important challenges, we consider this work to be a complete success and a major breakthrough in chemical laser technology. In fact, supersonic AGIL is the first fully chemically driven chemical laser system since the invention of COIL in 1978, more than 26 years ago. In principle, AGIL has the potential to be significantly more weight efficient than COIL because AGIL uses all gas-phase reagents. Moreover, because AGIL incorporates the same chemical combustor technology used by the HF/DF laser community, many of the issues related to building a large-scale, combustion-driven laser, including the use of high purity F_2, have already been addressed and/or solved. Thus, assuming that the issues

related to the safety of using high fluences of hydrogen azide can be overcome, the rapid development of high-energy AGIL devices should be forthcoming.

5. Acknowledgments

The authors acknowledge extensive helpful discussions with Prof. Michael Heaven (Emory University), Dr. Steven J. Davis (Physical Sciences, Inc.), Dr. William E. McDermott (Denver Research Institute), and Mr. Peter G. Crowell (Northrop Grumman, IT). The NCl($X^3\Sigma^-$) diagnostic was provided as a result of USAF SBIR funding via Contract F29601-00-C-0053. Finally, the supersonic AGIL program has benefited in countless ways from the hard work, dedication, and skills of Ms. Norma McMackin, Mr. Richard Dow, and Mr. Richard Hagenloh.

Note added in proof: A comprehensive final report that includes postsubmission results is available by request. The report is also available via the Defense Technical Information Center (DTIC)'s Scientific and Technical Information Network (STINET), under report number ADA430093.

References

[1]Becker, A.C., and U. Schurath, Chem. Phys. Lett. **160**, 586 (1989).

[2]Benard, D.J., M.A. Chowdhury, B.K. Winker, T.A. Seder, and H.H. Michels, J. Phys. Chem. **94**, 7507 (1990).

[3]Bower, R.D., and T.T. Yang, J. Opt. Soc. Am. B **8**, 1583 (1991).

[4]Clyne, M.A.A., and A.J. MacRobert, J. Chem. Soc. Faraday Trans. 2, **79**, 283 (1983).

[5]Clyne, M.A.A., A.J. MacRobert, J. Brunning, and C.T. Cheah, J. Chem. Soc. Faraday Trans. 2 **79**, 1515 (1983).

[6]Clyne, M.A.A., A.J. Macrobert, and L.J. Stief, J. Chem. Soc. Faraday Trans. Ii **81**, 159 (1985).

[7]Davis, S.J., W.J. Kessler, and M. Bachmann, Proc. SPIE **3612**, 157 (1999).

[8]Davis, S.J., W.J. Kessler, and P.B. Keating, Proc. SPIE **3931**, 156 (2000).

[9]Davis, S.J., P.A. Mulhall, W.J. Kessler, M.C. Heaven, and G.C. Manke II, Proc. SPIE **4971** (2003).

[10]Du, K.Y., and D.W. Setser, J. Phys. Chem. **94**, 2425 (1990).

[11]Duo, L., S. Tang, J. Li, X. Min, F. Sang, and B. Yang, Proc. SPIE **4631** (2002).

[12]Exton, D.B., J.V. Gilbert, and R.D. Coombe, J. Phys. Chem. **95**, 2692 (1991).

[13]Gilbert, J.V., X.L. Wu, D.H. Stedman, and R.D. Coombe, J. Phys. Chem. **91**, 4265 (1987).

[14]Heaven, M.C., Chemical Dynamics in Chemical Laser Media, in R.A. Dressler (ed.), *Chemical Dynamics in Extreme Environments, Advanced Series in Physical Chemistry*, World Scientific (2001).

[15]Henshaw, T.L., S.D. Herrera, G.W. Haggquist, and L.A.V. Schlie, J. Phys. Chem. A **101**, 4048 (1997).

[16]Henshaw, T.L., S.D. Herrera, and L.A.V. Schlie, J. Phys. Chem. A **102**, 6239 (1998).

[17]Henshaw, T.L., G.C. Manke II, T.J. Madden, M.R. Berman, and G.D. Hager, Chem. Phys. Lett. **325**, 537 (2000).

[18]Herbelin, J.M., T.L. Henshaw, B.D. Rafferty, B.T. Anderson, R.F. Tate, T.J. Madden, G.C. Manke, and G.D. Hager, Chem. Phys. Lett. **299**, 583 (1999).

[19]Hewett, K.B., G.C. Manke II, D.W. Setser, and G. Brewood, J. Phys. Chem. A **104**, 539 (2000).

[20]Hewett, K.B., and D.W. Setser, J. Phys. Chem. A **102**, 6274 (1998).

[21]Komissarov, A.V., G.C. Manke II, S.J. Davis, and M.C. Heaven, Proc. SPIE **3931** (2000).

[22]Komissarov, A.V., G.C. Manke II, S.J. Davis, and M.C. Heaven, J. Phys. Chem. A **106**, 8427 (2002).

[23]Lasing on the AGIL 1 and 2 devices was achieved with $g = (1-4) \times 10^{-4}$ cm^{-1} and the recent ElectriCOIL lasing demonstration by Carroll and coworkers was accomplished with $g = 6 \times 10^{-5}$ cm^{-1}.

[24]Manke, G.C., II, unpublished results (2004).

[25]Manke, G.C., II, C.B. Cooper, S.C. Dass, T.J. Madden, and G.D. Hager, IEEE J. Quant. Elect. **39**(8), 995 (2003).

[26]Manke, G.C., II, T.L. Henshaw, C.B. Cooper, and G.D. Hager, Recent Progress in the Development of a Multi-Watt All Gas-Phase Iodine Laser (AGIL), 33rd AIAA Plasmadynamics and Lasers Conference, Maui, HI (2002).

[27]Manke, G.C., II, T.L. Henshaw, T.J. Madden, and G.D. Hager, Chem. Phys. Lett. **310**, 111 (1999).
[28]Manke, G.C., II, T.L. Henshaw, T.J. Madden, and G.D. Hager, J. Phys. Chem. A **104**, 1708 (2000).
[29]Manke, G.C., II, T.L. Henshaw, T.J. Madden, J.M. Herbelin, B.D. Rafferty, and G.D. Hager, AIAA J. **39**, 447 (2001).
[30]Manke, G.C., II, and D.W. Setser, J. Phys. Chem. A **102**, 153 (1998).
[31]Manke, G.C., II, and D.W. Setser, J. Phys. Chem. A **102**, 7257 (1998).
[32]McDermott, W.E., Proc. SPIE **4631** (2002).
[33]McDermott, W.E., N.R. Pchelkin, D.J. Benard, and R.R. Bousek, Appl. Phys. Lett. **32**, 469 (1978).
[34]Ray, A.J., and R.D. Coombe, J. Phys. Chem. **97**, 3475 (1993).
[35]Ray, A.J., and R.D. Coombe, J. Phys. Chem. **99**, 7849 (1995).
[36]Schwenz, R.W., J.V. Gilbert, and R.D. Coombe, Chem. Phys. Lett. **207**, 526 (1993).
[37]25 Years of COIL, Sessions 1–3, Proc. SPIE **4631** (2002).
[38]Yang, T.T., V.T. Gylys, R.D. Bower, and L.F. Rubin, Opt. Lett. **17**, 1803 (1992).
[39]Zhao, Y., and D.W. Setser, J. Chem. Soc. Faraday Trans. **91**, 2979 (1995).